AIAA Aviation
13-17 June 2016, Washington, D.C.
34rd AIAA Applied Aerodynamics Conference

2016-3132

Computational Study of a Lifting Surface in Propeller Slipstreams

Sparsh A. Chadha,* Brent W. Pomeroy,† and Michael S. Selig‡
University of Illinois at Urbana-Champaign, Department of Aerospace Engineering, Urbana, IL 61801

The high speed flow in the wake of the propeller also known as propeller wash, or simply propwash, can severely affect the aerodynamic forces on a lifting surface. Steady-state computational results for a symmetric SD8020 airfoil of unit chord in a propeller slipstream at a freestream Reynolds number of 100,000 are presented in this paper. For the two-dimensional analysis, a propeller with a diameter-to-chord ratio of 1 was modeled as an actuator disk line with a pressure jump boundary condition varying from 1 to 4 lb/ft^2. As compared with the clean configuration, the lift coefficient and drag coefficient increased by a factor of five and 25, respectively, for the strongest actuator disk line configuration. The two-dimensional lift curve remained linear throughout the angle of attack range from 0 to 12 deg, and aerodynamic stall was not observed for the computed cases. Three-dimensional simulations with a circular actuator disk and a rectangular span lifting surface with a semi-span of unit chord were executed. Due to the wall mirroring effect, the setup simulated a system with infinite propellers upstream of a lifting surface with infinite span. A strong spanwise variation of lift in the slipstream shear layer resulted in induced trailing vortices. The trailing vortices caused downwash on the sections within the slipstream flow and upwash on the sections located outside the slipstream which led to an early onset of stall on the outboard sections.

Nomenclature

b	=	lifting surface span
C_a	=	axial force coefficient
$C_{a,f}$	=	axial force coefficient due to friction force
$C_{a,p}$	=	axial force coefficient due to pressure force
C_D	=	three-dimensional drag coefficient
C_d	=	two-dimensional drag coefficient
$C_{d,f}$	=	two-dimensional drag coefficient due to friction force
$C_{d,p}$	=	two-dimensional drag coefficient due to pressure force
C_f	=	skin friction coefficient
C_L	=	three-dimensional lift coefficient
C_l	=	two-dimensional lift coefficient
$C_{l,f}$	=	two-dimensional lift coefficient due to friction force
$C_{l,p}$	=	two-dimensional lift coefficient due to pressure force
C_n	=	normal force coefficient
$C_{n,f}$	=	normal force coefficient due to friction force
$C_{n,p}$	=	normal force coefficient due to pressure force
C_p	=	pressure coefficient
C_T	=	thrust coefficient
c	=	chord
D_A	=	actuator disk diameter
D	=	drag force
h	=	average grid size
L	=	lift force

*Graduate Student, Department of Aerospace Engineering, 104 S. Wright St., AIAA Student Member.
†Graduate Research Fellow, Department of Aerospace Engineering, 104 S. Wright St., AIAA Student Member.
‡Professor, Department of Aerospace Engineering, 104 S. Wright St., AIAA Associate Fellow.

N = number of cells
n = propeller speed (revolutions per second)
O = apparent order
r = grid refinement factor
Re = Reynolds number
S = lifting surface area
T = actuator disk thrust
V = velocity
V_r = relative velocity
w = velocity induced by the actuator disk
x = Cartesian coordinate parallel to freestream flow
y = chord-normal Cartesian coordinate
z = spanwise Cartesian coordinate
α = angle of attack
α_i = induced angle of attack
ΔA_i = area of i^{th} cell
ΔP = actuator disk pressure jump (lb/ft^2)
ε = relative error
ρ = density
Γ = circulation distribution
Ω = propeller speed (RPM)
ψ = error bound

Subscripts
ls = pertaining to the lower surface of the airfoil
us = pertaining to the upper surface of the airfoil
q = grid number
∞ = freestream conditions

I. Introduction

There has been a steady growth in demand for small-scale unmanned aerial vehicles (UAVs) and micro aerial vehicles (MAVs) in last two decades due to a breakthrough in miniature electronic components. Small-scale UAVs find specific military and civilian applications such as carrying payloads or undertaking surveillance and reconnaissance missions of an affected area. An understanding of high angle of attack aircraft flight dynamics and aerodynamic performance of these vehicles has been a subject of growing interest.[1]

The flowfield over the wing of a UAV or MAV is complicated by slipstream from a forward-mounted propeller over a low-aspect-ratio wing.[2] Since a major section of UAV wings lie in the wake of a propeller, the aerodynamic performance and stability is significantly affected by propwash. For a fixed-wing aircraft with a tractor propeller configuration, the integration aspect which has the greatest impact on overall aerodynamic performance is the interaction between propeller and wing.[3]

Recent experimental studies on slipstream effects of propellers on wings in low Reynolds number flow have shown significant performance benefits.[4,5] The aerodynamic coefficients of a lifting surface in low Reynolds number flow are dictated primarily by the formation, movement, and bursting of the laminar separation bubble.[2] Performance gains due to propeller/wing interaction in this flow regime are partially attributed to the absence of a laminar-separation bubble, thus resulting in improved aerodynamic efficiency and delayed stall.[5,6]

The slipstream flow of a propeller is simplified by considering two primary components of induced velocity. The axial velocity component is mainly steady and is well predicted by inviscid theories such as actuator disk theory, but the tangential component of the induced velocity (swirl of the propeller) is an unsteady phenomenon due to propeller rotation. When a lifting surface is located downstream of a propeller, these induced velocity components can significantly alter the aerodynamic forces on the lifting surface.[3,7–11] The lift and drag force on the lifting surface are directly affected by the increase in dynamic pressure due to the axial component of the induced velocity. The tangential component of the induced velocity as seen by the lifting surface changes with time. The downward-moving blade of the propeller, induces a downward component of velocity reducing lift on the section of the wing directly

downstream of the propeller, while the upward-moving blade induces an upward component of velocity and increases lift on the affected section. As a result, the lift continuously changes over one complete rotation. On the contrary, the presence of the lifting surface does not significantly affect the performance of the propeller blade as shown by both experimental and computational studies.[12,13]

The use of small distributed propellers upstream of the wing leads to an increase in aerodynamic lift.[14–17] The performance benefits of these wings are directly applicable to the takeoff and landing flight regimes due to a higher achievable lift curve slope and $C_{L_{max}}$. However, recent computational studies have shown the increase in aerodynamic drag of the wing due to slipstreams.[16,17] Wingtip mounted propellers which improve the aerodynamic efficiency of the wing[18,19] can be used to provide thrust during cruise with the inbound propeller shut and folded.[16] Preliminary wing design and aircraft performance tools for V/STOL aircraft with distributed propeller system such as those developed by Bronz et al.[20] require better theory to understand the aerodynamic interaction between a propeller and a wing.

The objective of this study was to carry out a simplified analysis of slipstream effects on a lifting surface in order to better understand the phenomenon of propeller/wing interaction. Two-dimensional computational methods were implemented to determine the reason for an increase in aerodynamic coefficients due to the slipstream of an actuator disk line on a symmetric SD8020 airfoil. In order to capture the impact of slipstream on spanwise variation of lift and drag coefficients, three-dimensional analyses with a circular actuator disk and rectangular span lifting surface were carried out. Additionally, this project has aimed to identify the relation between aerodynamic coefficients of the lifting surface due to pressure and friction force with angle of attack and pressure jump across actuator disk. A comparison of the coefficients in slipstream with the clean configuration gives a deep insight into aerodynamic interaction between propeller and the wing.

II. Two-Dimensional Analysis

A. ANSYS FLUENT

Aerodynamic analyses of the SD8020 symmetrical airfoil were carried out using the hybrid grid Reynolds Averaged Navier-Stokes solver, ANSYS FLUENT. The parallelized structured and unstructured node-based code, FLUENT, includes a pressure-based solver that was used for all the analyses. The pressure-based solver extracts the pressure field from continuity and momentum equations and the velocity field from the continuity equations. Several turbulence models without boundary layer transition are available in FLUENT: the Spalart Allmaras, the k-ε, and the k-ω. A turbulence model study was performed on these models because the boundary layer on a lifting surface in a propeller slipstream is fully turbulent.[5,19] FLUENT accepts structured and unstructured grids generated by ICEM CFD. For the current analyses, structured grids consisting of quadrilateral elements using a C-grid strategy around the airfoil were generated for the grid convergence study. Velocity inlet boundary conditions were used to specify the components of the freestream velocity based on Reynolds number and angle of attack as well as turbulence intensity of 0.01%. Far downstream of the airfoil, a pressure outlet boundary condition was used at the outlet of the computational domain to specify atmospheric pressure. The fan boundary condition at the location of actuator disk line was used to specify the value of pressure jump across the disk. In this paper, the configuration without the propeller is termed as "clean" and serves as a baseline for comparison.

B. Approach

The propeller was modeled as an interface with a pressure jump as is the case in actuator disk theory. From here on, the propeller is referred to as an actuator line for the two-dimensional analysis and as an actuator disk for the three-dimensional analysis. In order to observe strong slipstream effects on the airfoil, the diameter-to-chord ratio is set to unity. Based on the pressure jump, a certain amount of thrust is generated by the propeller as given by

$$T = \pi \left(\frac{D_A}{2} \right)^2 \Delta P \tag{1}$$

The thrust generated by the propeller can be non-dimensionalized using the rotation rate and diameter. The thrust coefficient is defined as

$$C_T = \frac{T}{\rho n^2 {D_A}^4} \tag{2}$$

The advance ratio of the propeller is the ratio of freestream velocity to the tip speed and is given by

$$J = \frac{V_\infty}{nD_A} \tag{3}$$

The induced axial velocity by the propeller can be calculated by actuator disk theory as

$$w = \frac{1}{2}\left[-V_\infty + \sqrt{{V_\infty}^2 + \frac{2\Delta P}{\rho}}\right] \tag{4}$$

A higher value of pressure jump produces a stronger induced velocity downstream of the actuator line. For a pressure jump value of 2 lb/ft^2 and freestream velocity of 15.72 ft/s, the slipstream velocity given by $V_\infty + 2w$ can be as high as three times the freestream velocity. The values of J and C_T can be obtained by assuming a reasonable propeller speed. Table 1 shows the summary of the above analysis performed at ΔP values of 1, 2, and 4 lb/ft^2. Table 1 shows that the current setup can simulate a real propeller with C_T values very close to the experimental values of small propellers at a given J.[21]

Once the computational solution is obtained, the aerodynamic coefficients can be obtained using the C_p and C_f distributions along the airfoil. The normal and axial force coefficients of the airfoil are calculated using

$$C_{n,p} = \int_0^c (C_{p,ls} - C_{p,us})\, d\left(\frac{x}{c}\right) \tag{5a}$$

$$C_{n,f} = \int_0^c (C_{f,ls} + C_{f,us})\, d\left(\frac{y}{c}\right) \tag{5b}$$

$$C_{a,p} = \int_0^c (C_{p,ls} - C_{p,us})\, d\left(\frac{y}{c}\right) \tag{5c}$$

$$C_{a,f} = \int_0^c (C_{f,ls} + C_{f,us})\, d\left(\frac{x}{c}\right) \tag{5d}$$

in which $C_{p,ls}$ and $C_{f,ls}$ are pressure and skin friction coefficients on the lower surface, and $C_{p,us}$ and $C_{f,us}$ are pressure and skin friction coefficients on the upper surface of the airfoil, respectively. The normal and axial force coefficients obtained by using the pressure coefficients are $C_{n,p}$ and $C_{a,p}$, and hence lift and drag coefficients obtained from these are called as pressure lift coefficient $C_{l,p}$ and pressure drag coefficient $C_{d,p}$ respectively. Similarly, $C_{n,f}$ and $C_{a,f}$ yield the friction lift coefficient $C_{l,f}$ and friction drag coefficient $C_{d,f}$.

The chordwise axial and normal forces are resolved in the direction parallel and perpendicular to freestream in order to obtain lift and drag forces using the airfoil angle of attack. Non-dimensionalization of the forces is done using the freestream dynamic pressure and airfoil chord length to obtain the aerodynamic coefficients. Expressions for the pressure lift and pressure drag coefficient as well as the friction lift and friction drag coefficient as obtained from the respective normal and axial force coefficients are given by

$$C_{l,p} = C_{n,p}\cos\alpha - C_{a,p}\sin\alpha \tag{6a}$$

$$C_{l,f} = C_{n,f}\cos\alpha - C_{a,f}\sin\alpha \tag{6b}$$

$$C_{d,p} = C_{n,p}\sin\alpha + C_{a,p}\cos\alpha \tag{6c}$$

$$C_{d,f} = C_{n,f}\sin\alpha + C_{a,f}\cos\alpha \tag{6d}$$

Table 1. Summary of Actuator Disk Analysis of the Current Setup

V_∞ (ft/s)	ΔP (lb/ft^2)	Ω (RPM)	C_T	J	w (ft/s)
15.72	1	3,500	0.10	0.27	8.6
15.72	2	4,700	0.11	0.20	14.1
15.72	4	6,000	0.13	0.16	22.2

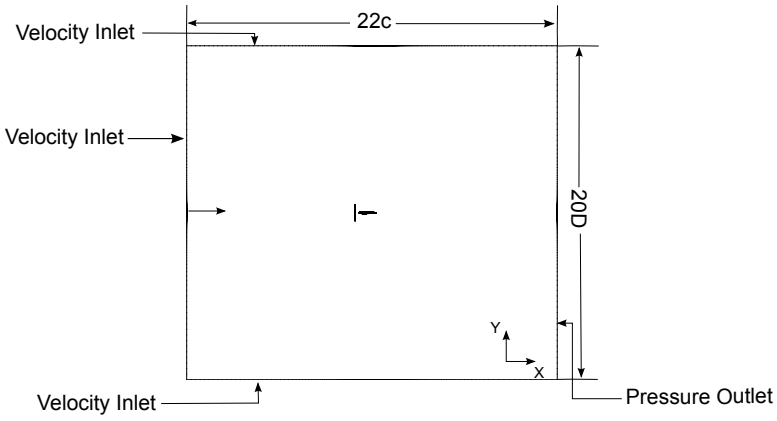

Figure 1. Schematic of the airfoil and actuator line geometry with labeled outer boundary conditions.

The airfoil lift coefficient C_l and drag coefficient C_d can be obtained by

$$C_l = C_{l,p} + C_{l,f} \tag{7a}$$

$$C_d = C_{d,p} + C_{d,f} \tag{7b}$$

Figure 1 shows the computational domain around the airfoil and actuator line (in center) along with the labeled outer boundary conditions. The airfoil of chord length 1 ft is vertically located on the center of the actuator line, and the leading edge is shifted horizontally by a distance of $0.25c$ in the downstream direction. Both the actuator line and the airfoil are assumed to be fixed to a certain airframe and hence rotate together with a change in angle of attack. Instead of changing the geometry in the computational domain, the freestream velocity components in the x and y direction were specified at the velocity inlet boundaries to account for changes in angle of attack. The domain extends $12c$ downstream of the actuator line and $10c$ upstream. Along the y direction, the domain extends $\pm 10D$ from the center of the actuator line. A Reynolds number of 101,700 was used for validation studies due to availability of experimental data, and a Reynolds number of 100,000 was used for all the remaining analysis cases.

C. Grid Convergence Study

A grid convergence study was performed by generating three structured C-grids consisting of only quadrilateral elements around the SD8020 airfoil in a clean configuration (no actuator line). The grid growth rate and the number of elements in the viscous boundary layer were the grid parameters that were varied to generate the three grids, and the details of the three grids are presented in Table 2.

Table 2. Grid Parameters for Grid Convergence Study

Grid Number q	Grid	Number of Cells	Grid Growth Rate (in the boundary layer)
1	Coarse	553,353	1.05
2	Medium	980,068	1.03
3	Fine	1,544,433	1.01

Figure 2 shows the grids around the leading edge with 5% chord and trailing edge with 0.7% chord of the airfoil. In order to accurately resolve the boundary layer flow and be compatible with the turbulence models, the maximum wall y^+ was kept at less than unity for all the three grids. Approximately 150 layers were generated in the boundary layer regions near the airfoil surface and were tightly stacked in order to maintain high resolution. Steady-state simulations using the SST k-ω turbulence model were run at a freestream Reynolds number of 101,700 and an angle of attack of 2.69 deg for which experimental data was available.[22]

A Grid Convergence Index (*GCI*) can be used to calculate the order of convergence.[23] This method provides an estimate of uncertainty in the converged solution and also indicates how the solution will change if the grid is refined

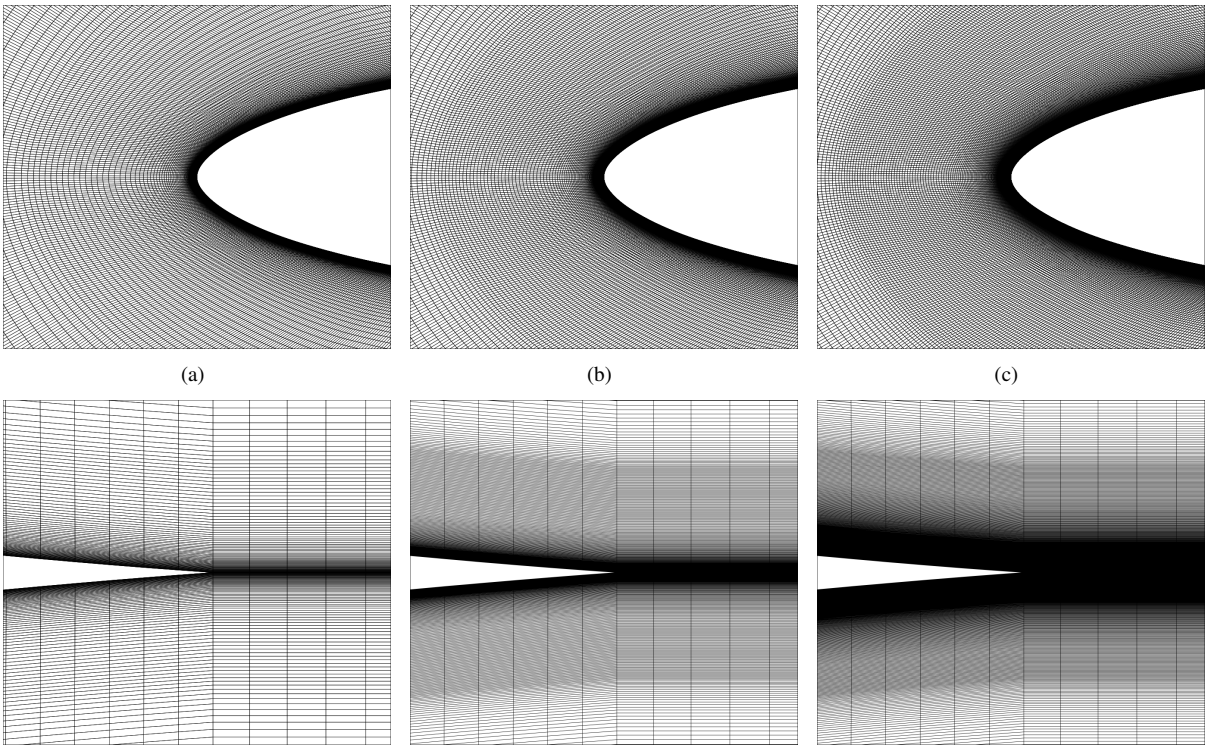

Figure 2. Grid around the leading edge of the airfoil with (a) coarse, (b) medium, and (c) fine density (forward 5% of the airfoil); trailing edge region with (d) coarse, (e) medium, and (f) fine density (aft 0.7% of the airfoil).

further. It is expected that the solution should approach an asymptotic value termed as the true numerical solution once the grid size is infinite. Average grid size was computed by

$$h = \left(\frac{1}{N} \sum_{i=1}^{N} \Delta A_i \right)^{\frac{1}{2}} \tag{8}$$

in which N is the total number of cells in the domain and ΔA_i is the area of the i^{th} cell. Next, the refinement factor of the grid was calculated using

$$r_{q,q+1} = \frac{h_q}{h_{q+1}} \tag{9}$$

in which the coarser grid is represented by q and the finer grid is represented by $q+1$. Transport equations have an apparent order O which was calculated by

$$O = \frac{1}{\ln(r_{q-1,q})} \ln \left[\left(\frac{C_{d_{q-1}} - C_{d_{q-2}}}{C_{d_q} - C_{d_{q-1}}} \right) \right] \tag{10}$$

The total number of grids used for the validation process arranged in increasing order of fineness is represented by q. The extrapolated solution for an infinitely dense mesh was obtained by using Richardson's extrapolation as

$$C_{d_\infty} = \frac{r_{q-1,q}^{O} C_{d_q} - C_{d_{q-1}}}{r_{q-1,q}^{O} - 1} \tag{11}$$

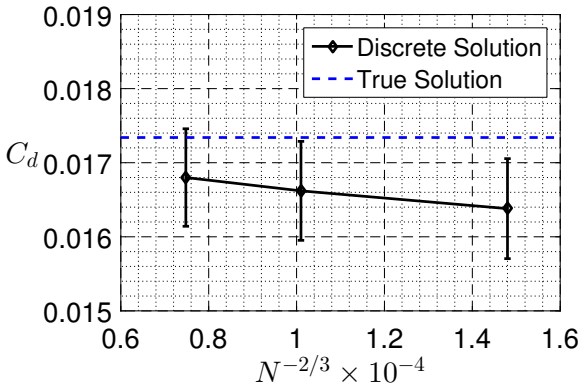

Figure 3. Grid convergence of C_d for SD8020 at Re = 101,700 and α = 2.69 deg.

The relative error based on the finite grid solutions was obtained by

$$\varepsilon_{rel} = \left| \frac{C_{d_q} - C_{d_{q-1}}}{C_{d_q}} \right| \tag{12}$$

Based on the true solution, the extrapolated relative error was calculated using

$$\varepsilon_{\infty} = \left| \frac{C_{d_\infty} - C_{d_q}}{C_{d_\infty}} \right| \tag{13}$$

Finally, the *GCI* was determined from the following expression

$$GCI = \frac{FOS\varepsilon_{rel}}{r^{O}_{q-1,q} - 1} \tag{14}$$

The factor of safety (FOS) was taken as 1.25 for the current analysis. The positive and negative error bounds were calculated from the *GCI* values obtained by using the fine and medium grid solutions. The expression for calculating the bounds is as follows

$$\psi = GCI \times C_{d_q} \tag{15}$$

A summary of this analysis is presented in Table 3, and the results are shown in Fig. 3. The finest grid is closest to the true solution. However, in order to save computational time, the medium sized mesh is used for future computations. The true solution is almost within the uncertainty bounds of the medium grid solution. Hence grid parameters similar to the medium sized grid around the airfoil with an addition of an actuator line were used for future computations after the selection of turbulence model. Figure 4 shows the final mesh around the airfoil and the actuator line with 2,020 nodes on the surface of the airfoil. The total number of cells in the computational domain are 1,235,133. The cells are concentrated near the leading and trailing edge of the airfoil with first cell height set at $y = 1\times10^{-5}$ ft with an airfoil chord of 1 ft.

Table 3. Summary of the Grid Convergence Study

Grid	Total Number of Cells (N)	$N^{-(2/3)}$	C_d Computational	C_d Richardson's Extrapolation	*GCI*	Bounds
Coarse	553,353	14.8×10^{-5}	0.01638	0.01734	0.04	6.58×10^{-4}
Medium	980,068	10.1×10^{-5}	0.01662	0.01734	0.04	6.68×10^{-4}
Fine	1,544,433	7.48×10^{-5}	0.01680	0.01734	0.04	6.75×10^{-4}

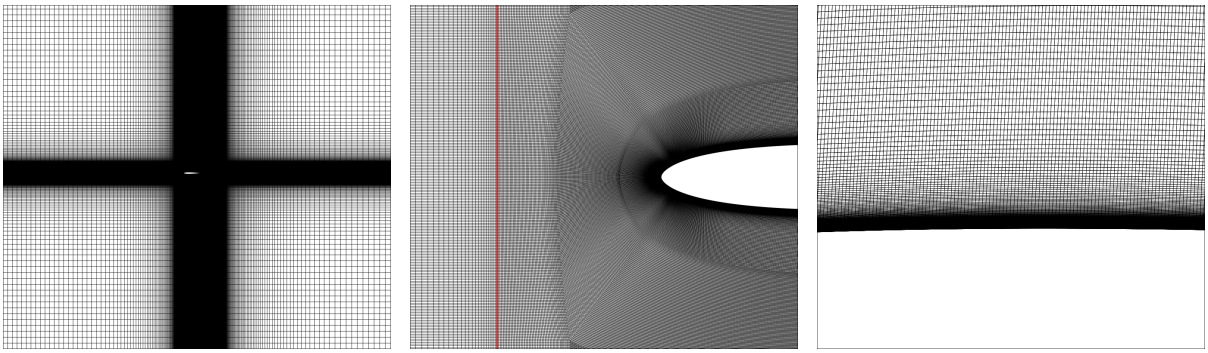

(a) (b) (c)

Figure 4. Final mesh around the airfoil and the actuator line: (a) entire computational domain, (b) grid near the airfoil leading edge (20% airfoil chord shown) and actuator line (red), (c) element growth near the airfoil upper surface (7% airfoil chord shown).

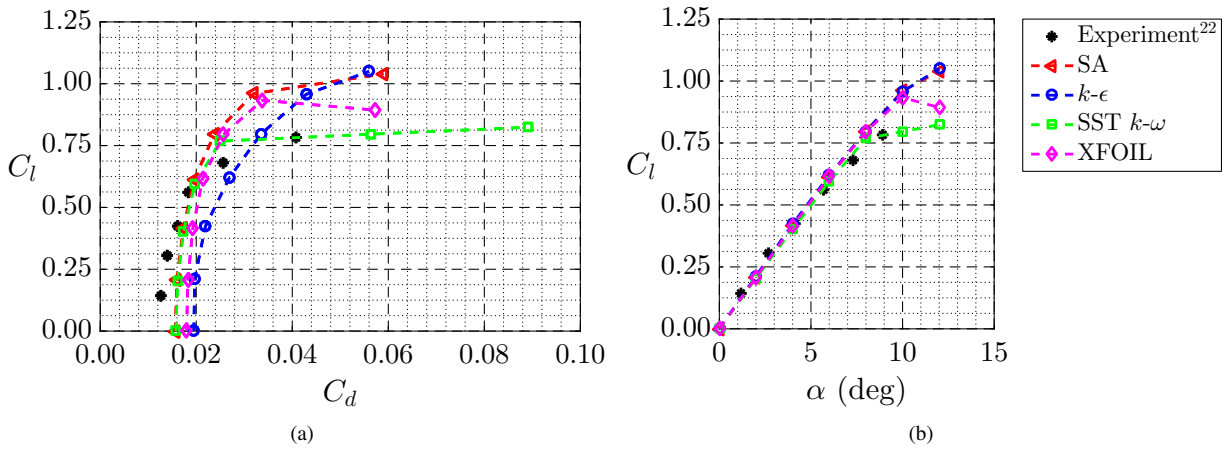

(a) (b)

Figure 5. Comparison of airfoil aerodynamic coefficients obtained from different turbulence models in ANSYS FLUENT with experiment and XFOIL at Re = 101,700 with (a) drag polars and (b) lift curves.

D. Turbulence Model Selection

The selection of the turbulence model is driven by computational cost and solution accuracy. Modeling boundary layer transition is not necessary for the two-dimensional analysis as the slipstream results in fully-turbulent flow over the airfoil sections situated inside it. As a result, the turbulence models available in FLUENT, which treat the boundary layer completely turbulent, were used to obtain the aerodynamic coefficients. The three fully-turbulent models available in FLUENT are Spalart-Allmaras,[24] k-ε,[25] and SST k-ω[26] turbulence models.

Computational data in a clean configuration were obtained at a freestream Reynolds number of 101,700 using the converged grid and compared with previously-collected experimental data[22] and fully-turbulent boundary layer runs in XFOIL. The fully-turbulent boundary layer runs in XFOIL were obtained by using forced transition at the stagnation point in order to have a completely turbulent boundary layer without a laminar separation bubble. Figure 5 shows the comparison of the aerodynamic coefficients obtained from CFD, XFOIL, and experiment. The airfoil drag coefficients as obtained from CFD and XFOIL fully-turbulent runs are higher than experimental values at low angles of attack as can be seen in Fig. 5(a). However, the polar from fully-turbulent XFOIL runs and the SST k-ω turbulence model agree fairly well for angles of attack below 8 deg. At high angles of attack, the airfoil polar from experiments and SST k-ω model show close resemblance.

The airfoil lift coefficient from CFD matches well for all the turbulence models in the prestall range below an angle of attack of 8 deg as can be seen in Fig. 5(b). Fully-turbulent lift coefficient from XFOIL and other turbulence models have a higher $C_{l_{max}}$ as compared with the experiments except SST k-ω model, which captures stall and agrees

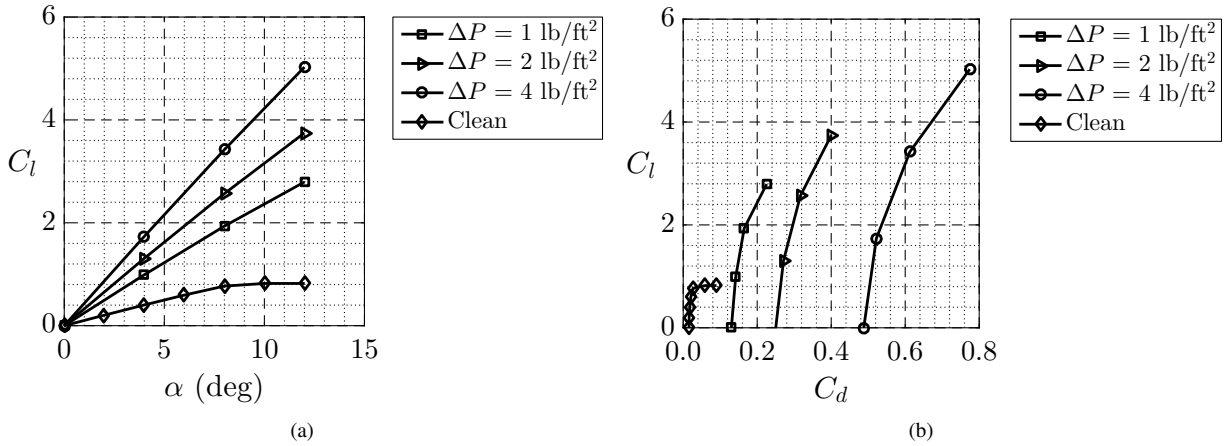

Figure 6. Comparison of SD8020 aerodynamic performance data for ΔP of 1, 2, and 4 lb/ft^2 and Re = 100,000 with the clean configuration as obtained from CFD: (a) lift curves and (b) drag polars.

well with the experimental values of C_l. As a result, for all future computations, the SST k-ω turbulence model was selected as a suitable turbulence model providing reasonable solution accuracy.

III. Two-Dimensional Results and Discussion

Computational analysis of the SD8020 airfoil at a Reynolds number of 100,000 for both the clean configuration as well as the one which contains the actuator line was carried out to obtain the lift and drag coefficients. The angle of attack was changed from 0 to 12 deg in steps of 2 deg for the clean configuration and in steps of 4 deg for the configurations with the actuator line. For the cases with the actuator line, the pressure jump values were 1, 2, and 4 lb/ft^2. As part of post-processing, the aerodynamic coefficients obtained from C_p and C_f distributions were analyzed using the lift curves and drag polars.

A. Lift Characteristics

Aerodynamic performance data, including lift curves and drag polars, are plotted for different pressure jumps across the actuator line and are shown in Fig. 6. From Fig. 6(a), it is evident that the airfoil lift coefficient increases with higher pressure jumps across the actuator line for a given angle of attack. As the pressure jump across the actuator line increases, it induces a stronger slipstream with a higher dynamic pressure. The airfoil, in the wake of the actuator line, is then immersed in a flow with high dynamic pressure and generates a higher lift. When this lift is non-dimensionalized using the freestream dynamic pressure which is lower than the slipstream dynamic pressure, a higher lift coefficient is obtained for a given α as seen in Fig. 6(a). Likewise, the lift curve slope also increases as the pressure jump across the actuator line increases.

Streamlines passing through the actuator line and the non-dimensionalized velocity magnitude contours, $\overline{V}$, at 12 deg airfoil angle of attack and ΔP of 2 lb/ft^2 are shown Fig. 7. As expected, the flow at angle of attack of 12 deg is turned in the direction that is more perpendicular to the actuator line. Thus, the flow as seen by the airfoil, situated in the wake of the actuator line, is at a lower angle than 12 deg. Velocity contours and streamlines in Fig. 7 indicate that the airfoil boundary layer is still attached. As a result, the lift coefficient does not drop for the configurations with the actuator line at angles of attack above 8 deg, and the lift curve exhibits a linear characteristic as seen in Fig. 6(a).

B. Drag Characteristics

Figure 6(b) shows the drag polar of the airfoil at Reynolds number of 100,000. Compared with the clean configurations, the C_d values of the airfoil with the actuator line are an order of magnitude higher. The drag coefficient increases with increasing pressure jump across the actuator line. The increase in airfoil drag coefficient due to the actuator line can be attributed to three major effects brought on by the actuator line slipstream on the airfoil as discussed in the following sections.

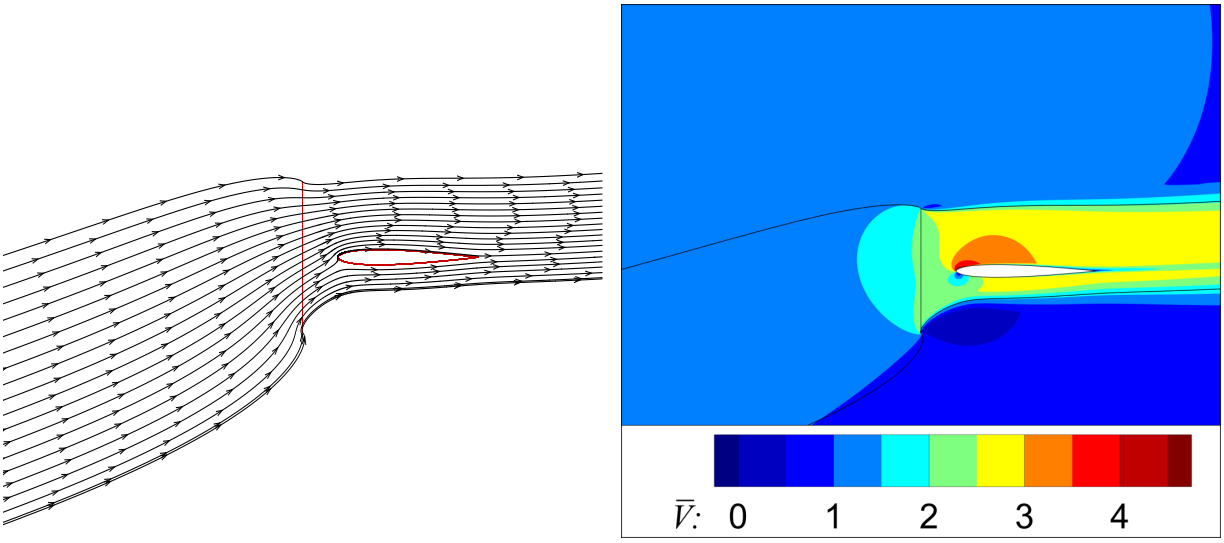

(a) (b)

Figure 7. Flow features around the airfoil for ΔP of 2 lb/ft^2 and 12 deg angle of attack: (a) streamlines passing through the actuator line and (b) non-dimensionalized velocity contours.

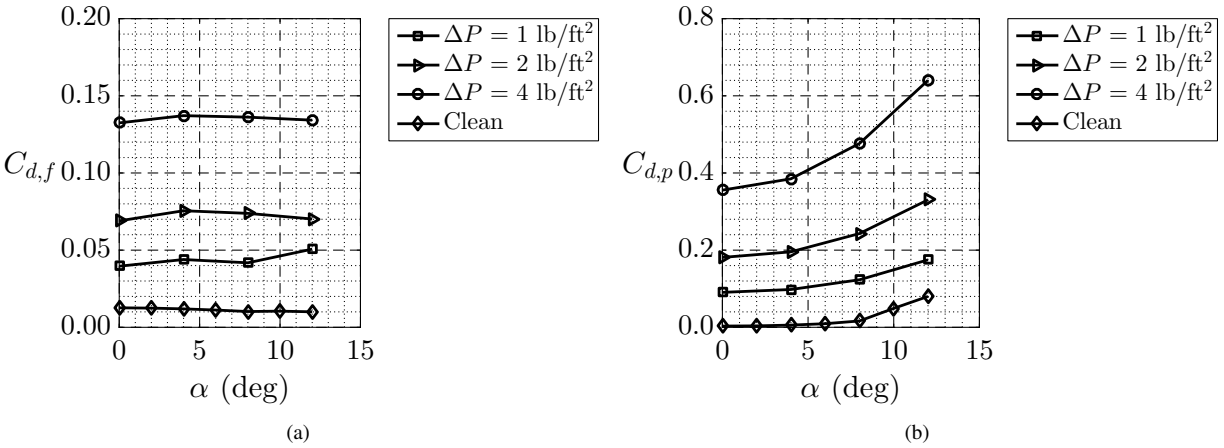

(a) (b)

Figure 8. Comparison of SD8020 drag at actuator line ΔP of 1, 2, and 4 lb/ft^2 and Re = 100,000 with the clean configuration as obtained from CFD in terms of (a) friction drag coefficient ($C_{d,f}$) and (b) pressure drag coefficient ($C_{d,p}$).

1. Local Velocity Effect

The slipstream of the actuator line has a velocity which is higher as compared with the freestream velocity. The Reynolds number obtained by using the velocity in the slipstream can be referred to as the local Reynolds number. This local *Re* is higher than the freestream *Re* value of 100,000. As discussed previously, the boundary layer is completely turbulent around the airfoil due to the propeller wash. The turbulent boundary layer and a higher dynamic pressure over the airfoil increases the friction force which, in turn increases the airfoil drag. Since the drag is non-dimensionalized by the freestream dynamic pressure, there is an increase in the drag coefficient as obtained from Eq. 6 relative to the clean configuration. As ΔP increases from 1 to 2 lb/ft^2, the velocity of the slipstream and hence the local dynamic pressure increases, thereby leading to a higher $C_{d,f}$ for all angles of attack as seen in Fig. 8(a). While there is a direct relationship between $C_{d,f}$ and ΔP, $C_{d,f}$ does not change significantly with angle of attack.

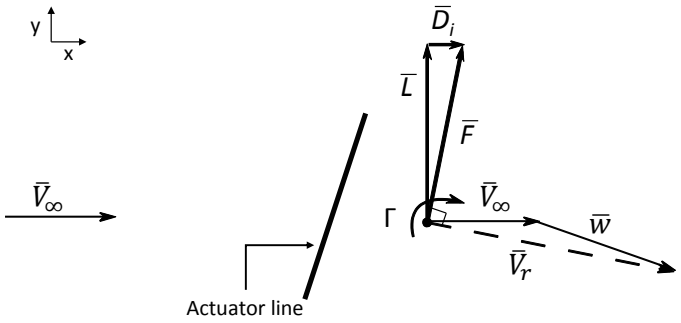

Figure 9. Tilting of force vector due to propeller slipstream resulting in an increase in drag of the airfoil.

2. Lift Vector Tilt Effect

In addition to the aforementioned velocity effect, increased drag also results from tilting of the lift vector. Figure 6(b) shows that the drag polar shifts to the right and gets stretched along C_l direction as ΔP is increased. For a ΔP of 4 lb/ft^2, C_d changes from 0.49 to 0.77 as α is changed from 0 to 12 deg. For the clean configuration, C_d increases from 0.016 to 0.090 for the same α change which is significantly less. The change in C_d with angle of attack, increases with increasing ΔP especially when the airfoil is producing non-zero lift thus indicating a contribution from the lift force toward the drag direction. Consider the case when the lifting airfoil is modeled as a single bound vortex at quarter chord location with circulation strength Γ generating a circulation force F. In this case, when the vortex is located in the wake of an actuator line, it experiences the flow as shown in Fig. 9.

An induced flow vector $\overline{w}$ due to the actuator line is added to the freestream flow $\overline{V}_\infty$ on the bound vortex. Consequently, the actual flow as seen by the airfoil is at a different local angle of attack than that of the freestream. Since drag is calculated along the freestream direction, a significant component of $\overline{F}$ contributes to drag, and this contribution is termed as induced drag, $\overline{D_i}$. The angle by which $\overline{F}$ gets tilted is a function of both the ΔP and α. As ΔP increases from 1 to 4 lb/ft^2, the magnitude of $\overline{w}$ increases to almost three times the freestream velocity leading to an increase in the tilting of $\overline{F}$ and ultimately $\overline{D_i}$. As α increases, the magnitude of the circulation force increases leading to a direct increase in $\overline{D_i}$. Thus, the increase in C_d with increasing α is significantly higher at non-zero lift values as compared with the clean configuration as shown in Fig. 6(b). The induced drag is absent when the airfoil is not generating any circulation force or lift.

3. Stagnation Pressure Effect

The final reason for an increase in C_d is the increase in pressure drag. The pressure jump across the actuator line increases the total pressure along streamlines downstream of the actuator line and results in a high speed slipstream. The streamlines with higher total pressure are imparted onto the airfoil situated in the wake of the actuator line. As a result, a higher pressure field, particularly around the airfoil leading edge is introduced which causes a significant increase in resultant force along the streamwise direction. Figure 10 shows a comparison of pressure forces acting along the airfoil with and without the actuator line at zero angle of attack. The red arrows indicate pressure forces acting toward the airfoil surface, and the blue arrows represent the pressure forces acting away from the airfoil surface.

Pressure drag can be obtained by resolving the pressure force around the airfoil along the streamwise direction. As seen in Fig. 10(b) the component of the forces indicated by the red arrows around the leading edge of the airfoil toward the drag direction increase when the airfoil has an actuator line upstream. As ΔP increases, the total pressure downstream of the actuator line increases, resulting in larger forces around the airfoil in the drag direction. As a result, C_d increases and the polar shifts to the right with increasing ΔP as seen in Fig. 6(b).

Larger pressure forces around the airfoil indicate a blown up C_p distribution around the airfoil. This scaling effect on C_p can be seen in Fig. 11. The contribution of C_p toward C_d is obtained using the pressure drag coefficient $C_{d,p}$ from Eq. 6b. At α of zero, the $C_{d,p}$ for airfoil in the wake of the actuator line is higher as compared with the clean configuration and increases with an increase in ΔP as can be seen in Fig. 8(b).

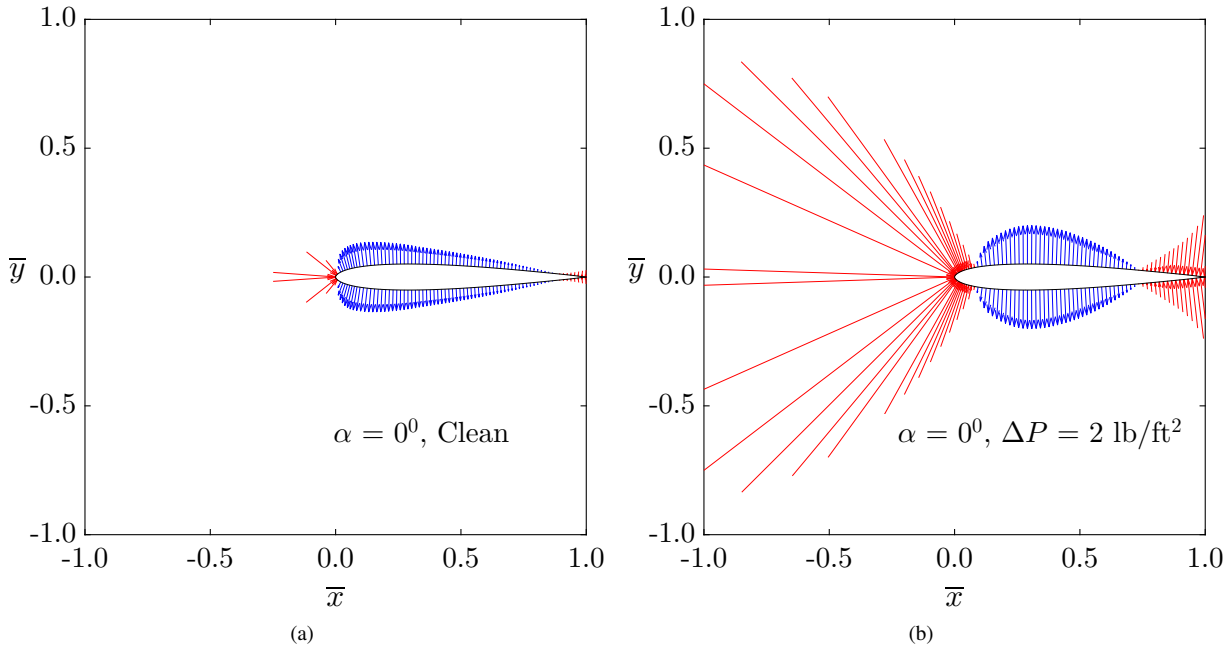

Figure 10. Comparison of pressure forces around the airfoil for $\alpha = 0$ deg and *Re* = 100,000: (a) absence and (b) presence of the actuator line.

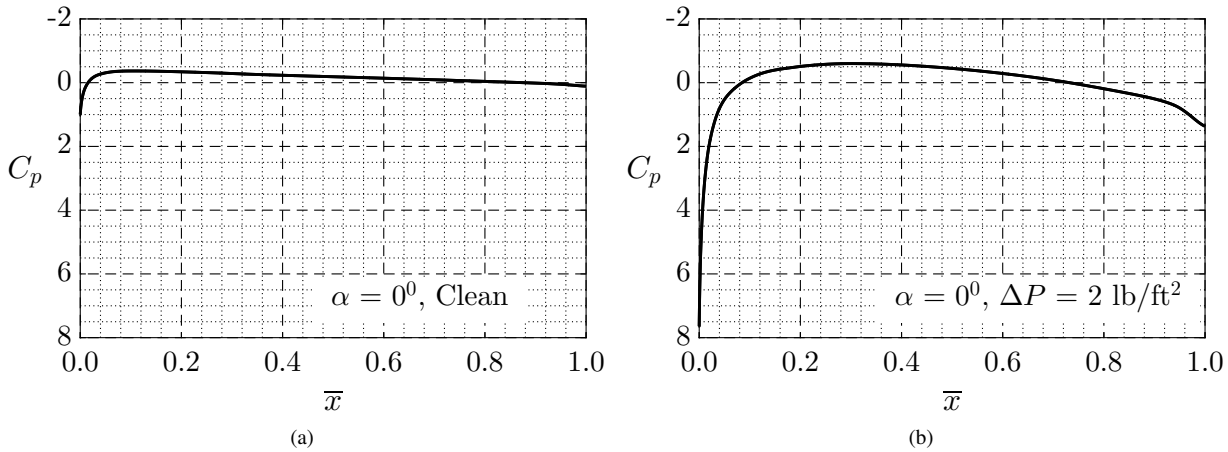

Figure 11. Comparison of C_p distribution around the airfoil for $\alpha = 0$ deg and *Re* = 100,000: (a) absence and (b) presence of the actuator line.

IV. Quasi Three-Dimensional Analysis

Two-dimensional computational analysis, although computationally inexpensive and informative from an airfoil-effects standpoint, does not represent the case of an actual aircraft wing located downstream of a propeller. The section of the wing located directly in the wake of the propeller lies in a slipstream whereas the remaining section is exposed to freestream flow. From the two-dimensional results presented in Sec. III, the airfoil sections located inside the slipstream will have higher lift and drag coefficients as compared with the airfoil sections located in the freestream flow. The sectional lift and drag coefficients will be dictated by the trailing vortices at the wing tips as well as the induced vortices generated due to the variation in bound circulation along the wing.

A. Computational Approach

Three-dimensional computational analyses were carried out in order to examine the effect of propeller wash on the lifting surface. In these analyses, the propeller with the D_A/c of 1 was modeled as a circular actuator disk with a pressure jump boundary condition. The airfoil geometry was extruded to have a fixed semi-span of c between two no-flux walls. Fig. 12(a) shows the top view of the geometry setup. The computational domain extends $22c$ along the x direction and $20D$ along the y direction similar to the two-dimensional domain as shown in Fig. 1. The distance between the leading edge of the lifting surface and the actuator disk is kept at $0.25c$, similar to the two-dimensional analysis.

A symmetry, or no-flux, boundary condition is implemented at the plane of symmetry shown in Fig. 12(a) to reduce computational costs. Due to the mirroring effects of the wall, the span of the lifting surface becomes infinite. However, the actuator disk is also mirrored and hence the current setup simulates an infinite propeller systems upstream of a rectangular lifting surface with infinite span. Despite the absence of wing-tip vortices, the actuator disk induces trailing vortices on the lifting surface, and hence this setup is termed as a quasi three-dimensional analysis. The airfoil section located at the plane of symmetry is termed as the center span, and the airfoil section located at the wall is termed as the end wall.

Post processing of the data involved calculation of the spanwise distribution of lift and drag coefficients as well as the induced angles of attack. The spanwise distribution of C_l and C_d can be obtained by using C_p and C_f of the airfoil sections. During this analysis, the spanwise distribution of $C_{d,p}$ and $C_{d,f}$ can also be obtained using Eq. 6. Using the spanwise lift distribution, the induced angle of attack at a particular z_0 location along the span is calculated using the lifting line equation as

$$\alpha_i(z_0) = \frac{1}{4\pi V_\infty} \int_{-b/2}^{b/2} \frac{d\Gamma/dz}{z_0 - z}\, dy \tag{16}$$

in which Γ is the bound circulation distribution along the span according to

$$\Gamma(z) = \frac{cC_l(z)V_\infty}{2} \tag{17}$$

The total three-dimensional lift (C_L) and drag (C_D) coefficient of the extended airfoil are obtained by integrating the sectional lift and drag coefficient values respectively over the entire span by

$$C_L = \frac{\int_{-b/2}^{b/2} c\, C_l\, dy}{\int_{-b/2}^{b/2} c\, dy} \tag{18a}$$

$$C_D = \frac{\int_{-b/2}^{b/2} c\, C_d\, dy}{\int_{-b/2}^{b/2} c\, dy} \tag{18b}$$

B. Grid and Solution Development

As a starting point in the development of the three-dimensional grid, the two-dimensional coarse grid was extruded along the lifting surface. In order to obtain a C-grid with low skew and high orthogonality around the rectangular-span lifting surface with an actuator disk in front of it, a multi-grid strategy was used. The fluid region upstream of the actuator disk was meshed independently from the cells in the downstream fluid region. The actuator disk was mapped using four quadrilateral blocks, and a uniform three dimensional C-grid was developed around the lifting surface. The mesh was refined in the boundary layer region to the extent that the elements were finely stacked with the first cell height of 10^{-5} ft and a grid growth rate of 1.04. The grid resolution in the wake was higher than the two-dimensional coarse grid but less than the medium grid due to computational limitations. The final mesh consisted of 45 spanwise nodes and had 14.3 million total hexahedral cells. Figure 13 shows the grid on the actuator disk and the lifting surface.

A coarse grid was generated with 9.4 million cells using the same grid technique but higher growth rate and less nodes on the lifting surface. In order to reduce computational costs, this coarse grid was used to obtain a low fidelity solution on a local machine with 8 GB of RAM and an Intel i7 processor clocked at 2.8 GHz. The SIMPLE scheme was used with first-order discretization of spatial derivatives to obtain the solution in approximately 24 hr. The low-fidelity

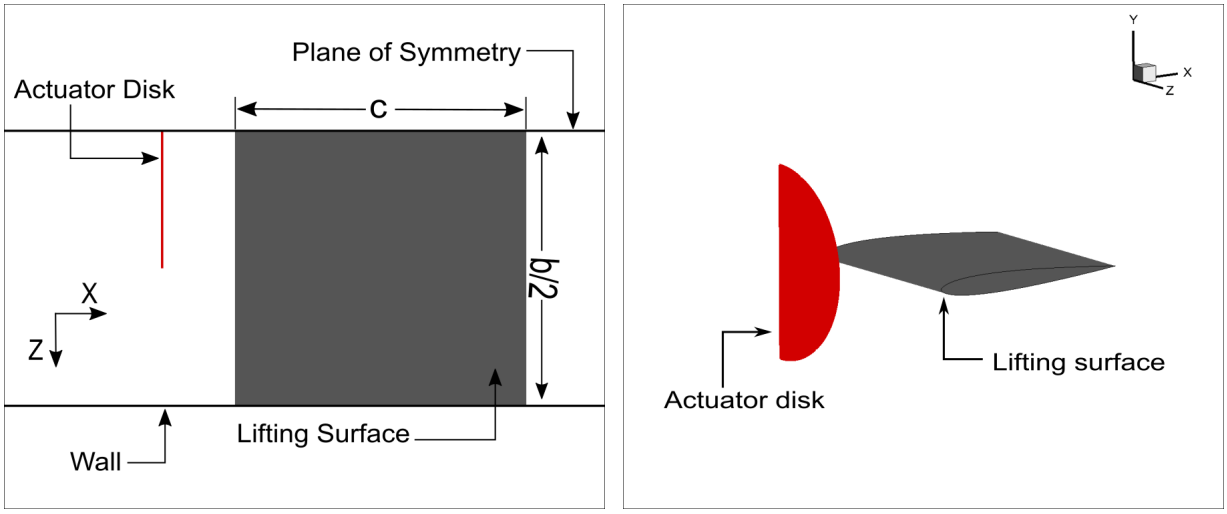

(a) (b)

Figure 12. The quasi three-dimensional geometry with the lifting surface and the actuator disk indicating the wall and the symmetry plane locations of the computational domain: (a) zoomed top view and (b) isometric view.

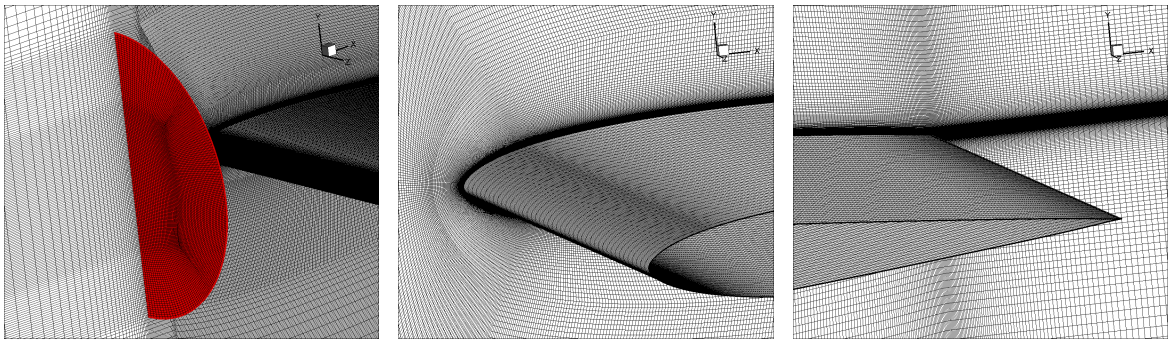

(a) (b) (c)

Figure 13. Final mesh around the (a) actuator disk (red), (b) lifting surface leading edge, and (c) lifting surface trailing edge.

solution was then interpolated onto the final mesh thus providing a better starting point for the final computations on the high-density grid and saving computational time. The Coupled scheme with second-order discretization of spatial derivatives was used to determine the high-fidelity solution. Batch jobs utilizing 14 processes and allocating 56 GB of RAM on the Illinois Campus Cluster consisting of Intel Xeon processors clocked at 2.67 GHz were used to obtain the final solution.

V. Three-Dimensional Results and Discussion

Three-dimensional CFD analyses were performed with the rectangular-span SD8020 lifting surface located downstream of an actuator disk. The pressure jump across the actuator disk varied from 1 to 2 lb/ft^2, and the angle of attack was changed from 0 to 8 deg in steps of 4 deg. The Reynolds number at which the analysis was performed was 100,000. Performance data in terms of spanwise lift and drag coefficients were obtained for all the cases.

A. Spanwise C_l Distribution

The spanwise variation of C_l for the actuator disk ΔP of 1 and 2 lb/ft^2 is shown in Fig. 14. Sections of the lifting surface located directly downstream of the actuator disk show higher total lift coefficient. The C_p distribution along the airfoil

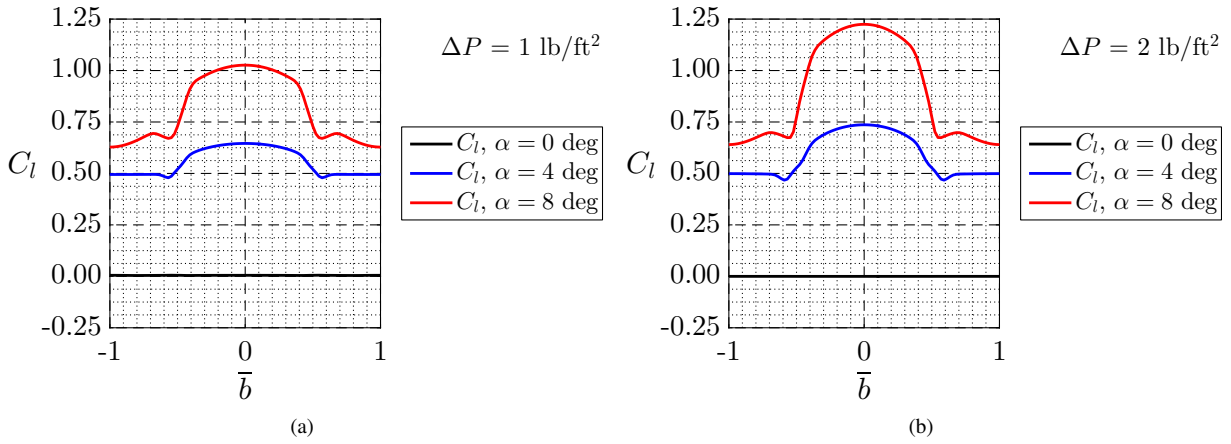

Figure 14. Comparison of spanwise C_l distribution for quasi three-dimensional configurations at Re =100,000: (a) ΔP = 1 lb/ft^2 and (b) ΔP = 2 lb/ft^2.

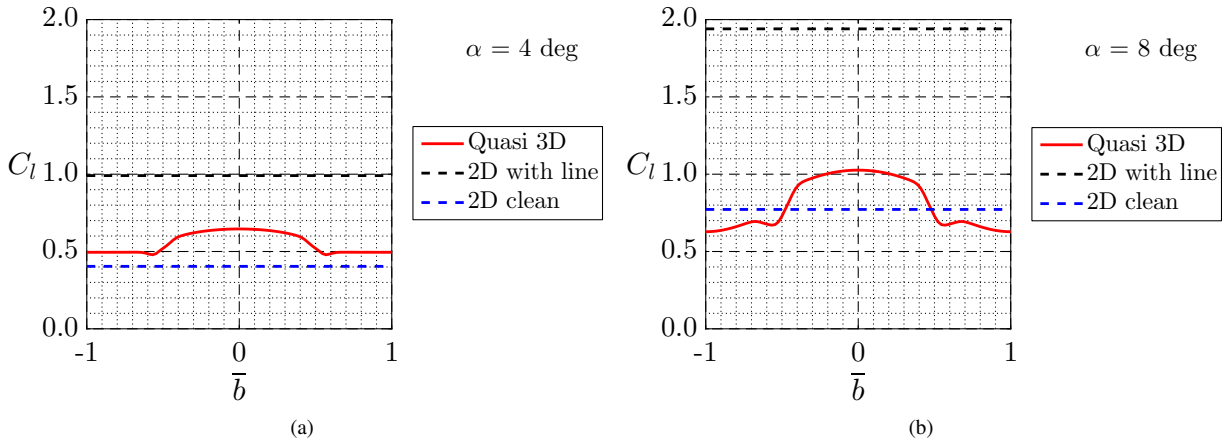

Figure 15. Comparison of spanwise C_l distribution for two-dimensional clean, two-dimensional with actuator disk, and quasi three-dimensional configurations at ΔP of 1 lb/ft^2: (a) α = 4 deg and (b) α = 8 deg.

section has the major contribution to C_l. The area under the C_p curve for airfoil sections located inside the actuator disk slipstream is higher than the outboard airfoil sections as discussed in Sec. III (B3). As a result, the sectional C_l decreases from the center span sections toward the end wall sections. The spanwise C_l continuously increases with angle of attack. Effects on the C_l near the center span increase with an increasing ΔP as can be seen by comparing Fig. 14(a) and Fig. 14(b).

A comparison of the two-dimensional clean, the two-dimensional with actuator line, and the quasi three-dimensional spanwise C_l of the lifting surface at angle of attack of 4 and 8 deg and ΔP of 1 lb/ft^2 is shown in Fig. 15. At angles of attack of 4 deg and 8 deg, near the center span region, the C_l obtained from the quasi three-dimensional analysis is less than the C_l obtained from the two-dimensional analysis with the actuator line. This observation indicates that the region of the lifting surface located in the wake of the actuator disk slipstream encounters a downwash which reduced the local angle of attack at these sections.

Near the end wall region and at angle of attack of 4 deg, the local C_l as obtained from quasi three-dimensional analysis is higher as compared to the clean configuration. This observation indicates that the regions located outside the slipstream of the actuator disk encounter an upwash that leads to an increase in local angle of attack at these sections. Figure 16 shows the spanwise distribution of induced angle of attack on the lifting surface obtained during the quasi three-dimensional analysis. This observation further confirms the presence of trailing vortices located at the edge of the actuator disk. These trailing vortices cause downwash in regions of the lifting surface located within the slipstream and upwash in regions located outside of it. For the angle of attack of 8 deg, the decreased local C_l of the

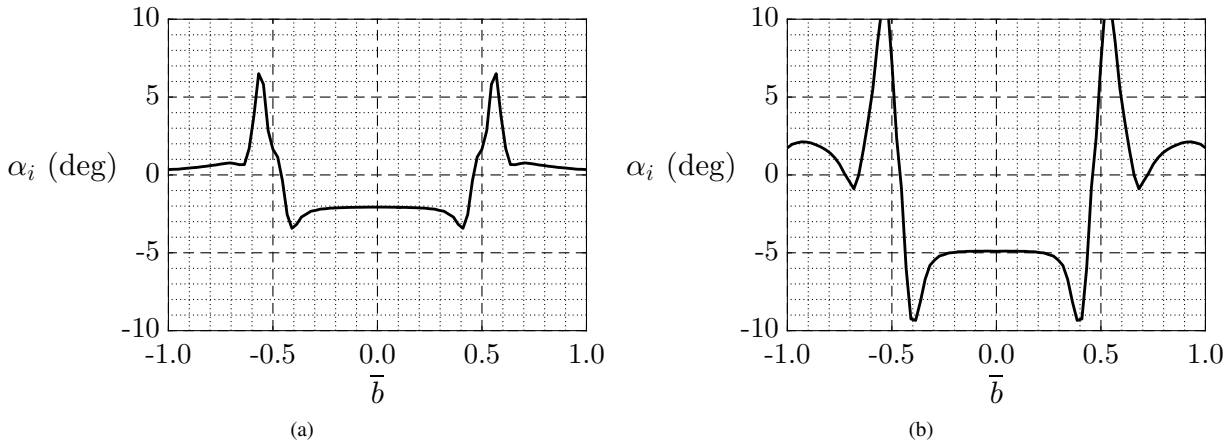

Figure 16. Comparison of spanwise α_i distribution on the lifting surface at ΔP of 1 lb/ft^2: (a) α = 4 deg and (b) α = 8 deg.

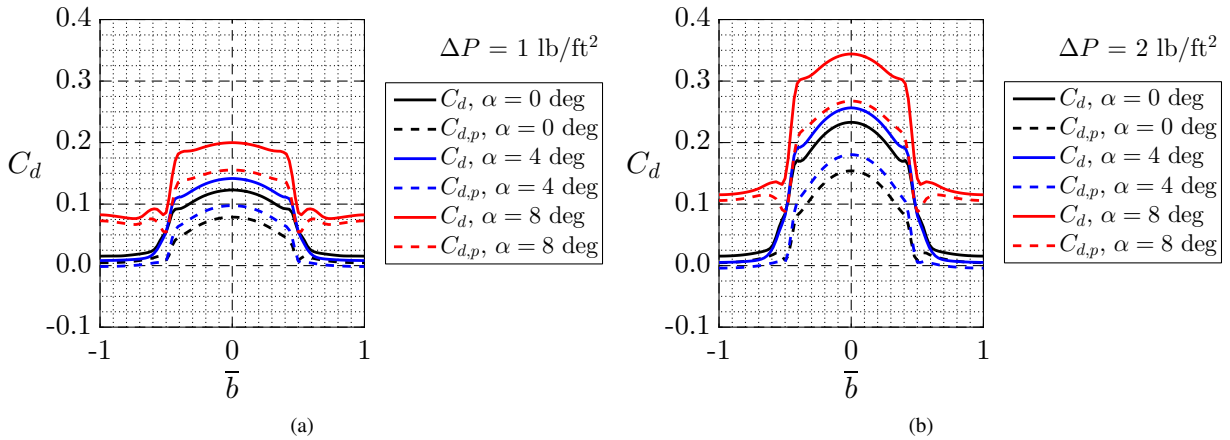

Figure 17. Comparison of spanwise C_d and $C_{d,p}$ distribution for quasi three-dimensional configurations at Re = 100,000: (a) ΔP = 1 lb/ft^2 and (b) ΔP = 2 lb/ft^2.

quasi three-dimensional lifting surface relative to the C_l of the clean configuration suggests that the airfoil region is stalled. Upwash from the trailing vortices increases the local angle of attack near the end wall relative to the clean configuration which leads to an earlier stall.

B. Spanwise C_d Distribution

Figure 17 shows the spanwise variation of C_d and $C_{d,p}$ for actuator disk ΔP of 1 and 2 lb/ft^2. The total drag coefficient is higher in regions directly behind the actuator disk and drops sharply in regions outside the actuator disk slipstream supporting the results in Sec. III. The effect on C_d near the center span regions increases with an increasing ΔP as can be seen by comparing Fig. 17(a) and Fig. 17(b).

A comparison of two-dimensional clean, two-dimensional with actuator line, and the quasi three-dimensional spanwise C_d of the lifting surface at angle of attack of 4 and 8 deg and ΔP of 1 lb/ft^2 is shown in Fig. 18. Near the end wall airfoil sections, at an angle of attack of 4 deg, C_d obtained from quasi three-dimensional analysis is less as compared with C_d of the clean configuration. This is because, the regions located outside of the slipstream encounter an upwash due to the induced vortices. The upwash creates induced thrust as opposed to induced drag, which reduces the C_d in these regions. The reduction in C_d at the endwall, however, does not occur for angle of attack of 8 deg because the boundary layer in these regions is separated leading to airfoil stall. The stalled sections encounter an increase in pressure drag as seen from the dotted lines in Fig. 17 for α of 8 deg near the end wall regions.

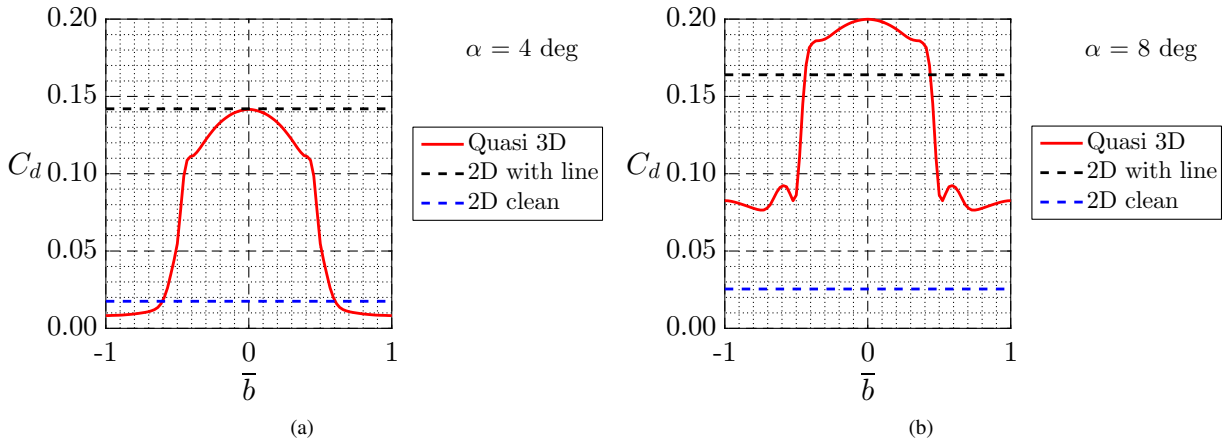

Figure 18. Comparison of spanwise C_d distribution for two-dimensional clean, two-dimensional with actuator line, and quasi three-dimensional configurations at ΔP of 1 lb/ft^2: (a) α = 4 deg and (b) α = 8 deg.

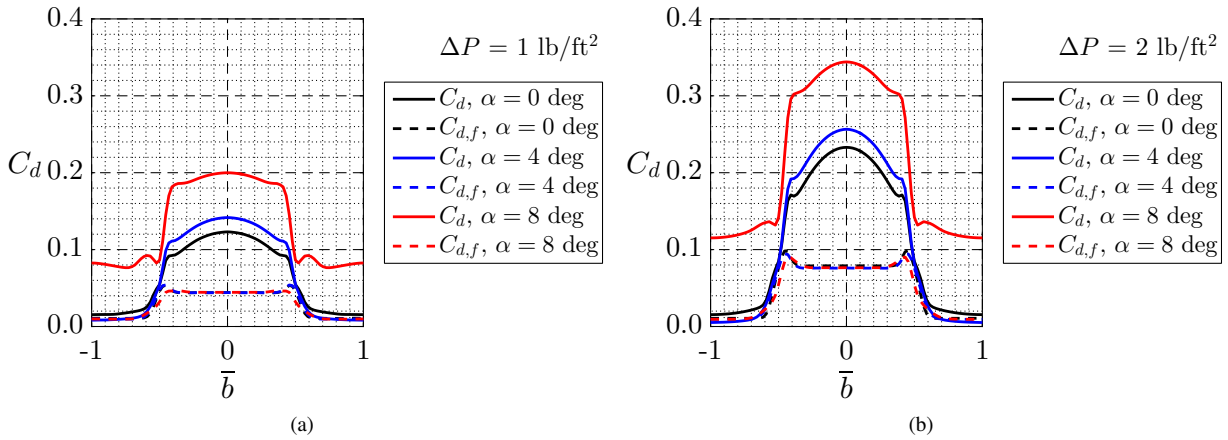

Figure 19. Comparison of spanwise C_d and $C_{d,f}$ distribution for quasi three-dimensional configurations at Re = 100,000: (a) ΔP = 1 lb/ft^2 and (b) ΔP = 2 lb/ft^2.

The regions located within the slipstream of the actuator disk for the quasi three-dimensional configuration have C_d comparable or even less than the two-dimensional configuration with actuator line. Since these regions encounter downwash, the local angle of attack is lower than the geometric angle of attack. From the polar in Fig. 6(b), it would be expected that they have a local C_d less than the two-dimensional C_d of the airfoil with actuator line. However, these sections now have an induced drag component due to the local downwash brought on by the trailing vortices whose strength increases with increase in α. As a result, the quasi three-dimensional C_d is almost equal to the two-dimensional C_d for α of 4 deg near the center span but becomes higher than the two-dimensional C_d at 8 deg as seen in Fig. 18. The spanwise C_d can be broken down in to the friction drag coefficient $C_{d,f}$ and pressure drag coefficient $C_{d,p}$. A discussion of observed trends in $C_{d,f}$ and $C_{d,p}$ is presented below.

1. Spanwise $C_{d,f}$ Distribution

The skin friction drag influences the value of the total C_d. Skin friction drag is relatively significant at low angles of attack. The dashed lines in Fig. 19 indicate that the regions located within the propeller slipstream show higher friction drag coefficients as compared with the wall regions. The primary reason for this change is due to increased local Reynolds number in regions directly behind the disk leading to a higher skin friction coefficient as discussed in Sec. III(B1). The $C_{d,f}$ distribution peaks near the edges of the actuator disk. While moving from the actuator disk

slipstream into freestream flow along the span, there exists a shear layer increasing the local shear in these regions. The increase in local shear due to the velocity gradient along the span increases the $C_{d,f}$ in these regions.

2. *Spanwise $C_{d,p}$ Distribution*

The pressure drag coefficient, as shown by the dashed lines in Fig. 17, contributes significantly to the total drag coefficient of the lifting surface. In the regions behind the actuator disk, $C_{d,p}$ is higher than the outer sections because the pressure field inside the slipstream is higher than the freestream flow. There is a sharp drop in $C_{d,p}$ between the airfoil sections in the slipstream and outside of it. In the regions located outside the actuator disk slipstream, there is a significant jump when α is changed from 4 to 8 deg. As previously mentioned, some boundary-layer separation is observed near the wall airfoil sections at α of 8 deg which lead to a higher $C_{d,p}$. Also, as compared with the $C_{d,p}$ at the wall airfoil sections, the center span $C_{d,p}$ increases significantly with angle of attack indicating an increasing contribution from the tilted circulation force vector toward drag as discussed in Sec. III(B2).

VI. Conclusions

From the two-dimensional computational analyses, it is evident that the lift and drag coefficients of the airfoil increase in presence of an actuator line as compared with the clean configuration. The slipstream effects presented in this paper highlight the reason for the increase in aerodynamic coefficients of the lifting surface situated in the wake of a propeller due to pressure and friction forces. An increase in pressure drag of the airfoil is a result of the pressure field introduced by the actuator line inside the slipstream. The high-speed flow of the propeller wash also causes the tilting of the lift vector in the downstream direction and results in drag due to lift termed as induced drag. Relatively higher fluid velocity in the slipstream as compared with the freestream, increases the dynamic pressure around the airfoil and thus leads to a higher C_d. An increase in lift due to the high-speed flow induced on airfoil surface by the actuator line is non-dimensionalized by freestream dynamic pressure. Consequently, the C_l at a given angle of attack and thereby the lift-curve slope both increase relative to the clean configuration. The airfoil section does not stall since the relative angle of attack does not reach high stall angles, and the lift-curve slope stays mainly linear throughout the angle of attack range of 0 to 12 deg. As the pressure jump across the actuator line increases, the increase in C_l and C_d becomes more significant.

Quasi three-dimensional analysis shows similar behavior of airfoil spanwise coefficients located in the propeller slipstream to the two-dimensional coefficients. Spanwise lift and drag coefficients are higher in regions located in the wake of the actuator disk as compared with the regions located outside the slipstream. Clean airfoil behavior with relatively lower aerodynamic coefficients and aerodynamic stall is observed in regions located outside the propeller slipstream. However, due to change in lift across the span, two strong counter-rotating trailing vortices are induced at the edge of the actuator disk slipstream on the lifting surface. These strong vortices introduce downwash in regions located within the propeller slipstream and lead to vortex-induced drag. The upwash in regions located outside the propeller slipstream affects the aerodynamic performance by introducing vortex-induced thrust and early onset of stall as compared with the clean configuration. The aerodynamic coefficients and their trends with increasing ΔP and α can show which effects are significant while considering propeller/wing interaction.

Acknowledgments

Support for this project was provided by the UIUC Department of Aerospace Engineering in addition to the UIUC College of Engineering. Additional support was provided by National Science Foundation graduate research fellowship grant number 07-15088. The authors would also like to acknowledge the UIUC Department of Computational Science and Engineering and the College of Engineering for providing essential computation time on the CSE Parallel Computing Resources hosted by the Illinois Campus Cluster.

References

[1]Selig, M. S., "Real-Time Flight Simulation of Highly Maneuverable Unmanned Aerial Vehicles," *J. of Aircraft*, Vol. 51, No. 6, 2014, pp. 1705–1725.

[2]Ananda, G. K., *Aerodynamic Performance of Low-to-Moderate Aspect Ratio Wings at Low Reynolds Numbers*, Master's thesis, Dept. of Aerospace Engineering, University of Illinois at Urbana-Champaign, Urbana, IL, 2012.

[3]Witkowski, D. P., Lee, A. K. H., and Sullivan, J., "Aerodynamic Interaction between Propellers and Wings," *J. of Aircraft*, Vol. 26, No. 9, 1989, pp. 829–836.

[4]Catalano, F. M., "On the Effects of an Installed Propeller Slipstream on Wing Aerodynamic Characteristics," *Acta Polytechnica*, Vol. 44, No. 3, 2004, pp. 8–14.

[5]Ananda, G. K., Deters, R. W., and Selig, M. S., "Propeller Induced Flow Effects on Wings at Low Reynolds Numbers," AIAA Paper 2013-3193, San Diego, CA, June 2013.

[6]Ananda, G. K., Deters, R. W., and Selig, M. S., "Propeller-Induced Flow Effects on Wings of Varying Aspect Ratio at Low Reynolds Numbers," AIAA Paper 2014-2152, Atlanta, GA, June, 2014.

[7]Jameson, A., "The Analysis of Propeller-Wing Flow Interaction," NASA SP-228, Oct. 1969, pp. 721–749.

[8]Kuhn, R. E. and Draper, J. W., "An Investigation of a Wing-Propeller Configuration Employing Large-Chord Plain Flaps and Large-Diameter Propellers for Low-Speed Flight and Vertical Take-Off," NACA TN 3307, Dec. 1954.

[9]Page, S. O., Deckert, V. R., and Dickinson, W. H., "Large-Scale Wind-Tunnel Tests of a Deflected Slipstream STOL Model with Wings of Various Aspect Ratios," NASA TN D-4448, Mar. 1968.

[10]Gamble, B. J. and Reeder, M. F., "Experimental Analysis of Propeller-Wing Interactions for a Micro Air Vehicle," *J. of Aircraft*, Vol. 46, No. 1, 2009, pp. 65–73.

[11]Schroijen, M. J. T., Veldhuis, L. L. M. and Slingerland R., "Propeller Empennage Interaction Effects on the Vertical Tail Design of Multi-engine Aircraft," *J. of Aircraft*, Vol. 47, No. 4, 2010, pp. 1133–1140.

[12]Fratello, G., Favier, D., and Maresca, C., "Experimental and Numerical Study of the Propeller/Fixed Wing Interaction," *J. of Aircraft*, Vol. 28, No. 6, 1991, pp. 365–373.

[13]Veldhuis, L. M. M., *Propeller-Wing Aerodynamic Interference*, Ph.D. Dissertation, Dept. of Aerospace Engineering, Delft University of Technology, Delft, The Netherlands, June 2005.

[14]Fu, W., Li, J., and Wang, H., "Numerical Simulation of Propeller Slipstream Effect on a Propeller-Driven Unmanned Aerial Vehicle," International Conference on Advances in Computational Modeling and Simulation, Vol. 31, pp. 150–155, 2012.

[15]Moore, M. D. and Fredericks, W. J., "Misconceptions of Electric Aircraft and Their Emerging Aviation Markets," AIAA Paper 2014-0535, Jan. 2014.

[16]Stoll, A. M., Bevrit, J., Moore, M. D., Fredericks, W. J., and Borer, N. K., "Drag Reduction through Distributed Electric Propulsion," AIAA Paper 2014-2851, June, 2014.

[17]Durai, A., "Experimental Investigation of Lift and Drag Characteristics of a Typical MAV under Propeller Induced Flow," *International Journal of Micro Air Vehicles*, Vol. 6, No. 1, 2014, pp. 63–72.

[18]Patterson, J. C. and Barlett, G. R., "Effect of a Wing-Tip Mounted Pusher Turboprop on the Aerodynamic Characteristics of a Semi-Span Wing," AIAA Paper 1985-1286, Monterey, CA, July 1985.

[19]Dimchev, M., *Experimental and Numerical Study on Wingtip Mounted Propellers for Low Aspect Ratio UAV Design*, Master's thesis, Dept. of Aerospace Engineering, Delft University of Technology, Delft, The Netherlands, 2012.

[20]Bronzl, M. and Drouin, A., "Preliminary Design Estimation of the V/STOL Airplane Performance," IMAV 2015, International Micro Air Vehicles Conference and Flight Competition, Aachen, Germany, September 2015.

[21]Deters, R. W., *Performance and Slipstream Characteristics of Small-Scale Propellers at Low Reynolds Numbers*, Ph.D. Dissertation, Dept. of Aerospace Engineering, University of Illinois at Urbana-Champaign, Urbana, IL, 2014.

[22]Selig, M.S., Guglielmo, J.J., Broeren, A.P., and Giguère, P., "Summary of Low-Speed Airfoil Data," Vol. 1, SoarTech Publications, Virginia Beach, VA, 1995.

[23]Celik, I., Ghia, U., Roache, P., and Freitas, C., "Procedure for Estimation and Reporting of Uncertainty Due to Discretization in CFD Applications," *Journal of Fluids Engineering*, Vol. 10, No. 7, July 2008, pp. 1–4.

[24]Spalart, P. R. and Allmaras, S. R., "A One-Equation Turbulence Model for Aerodynamic Flows," AIAA Paper 92-0439, 1992.

[25]Jones, W. P. and Launder, B. E., "The Prediction of Laminarization with a Two Equation Model of Turbulence," *International Journal of Heat and Mass Transfer*, Vol. 15, July 1972, pp. 301–314.

[26]Menter, F. R., "Two-Equation Eddy-Viscosity Turbulence Models for Engineering Applications," *AIAA Journal*, Vol. 32, No. 8, 1994, pp. 1598–1605.